Inner and outer electron diffusion region of antiparallel collisionless reconnection: Density dependence

Cite as: Phys. Plasmas **26**, 102305 (2019); https://doi.org/10.1063/1.5109368
Submitted: 08 May 2019 . Accepted: 12 September 2019 . Published Online: 14 October 2019

A. Divin, V. Semenov, I. Zaitsev, D. Korovinskiy, J. Deca, G. Lapenta, V. Olshevsky, and S. Markidis

Physics of Plasmas ARTICLE scitation.org/journal/php

Inner and outer electron diffusion region of antiparallel collisionless reconnection: Density dependence

Cite as: Phys. Plasmas **26**, 102305 (2019); doi: 10.1063/1.5109368
Submitted: 8 May 2019 · Accepted: 12 September 2019 ·
Published Online: 14 October 2019

A. Divin,[1,a)] V. Semenov,[1] I. Zaitsev,[1] D. Korovinskiy,[2] J. Deca,[3] G. Lapenta,[4] V. Olshevsky,[5] and S. Markidis[5]

AFFILIATIONS

[1]Department of Earth's Physics, St. Petersburg State University, St. Petersburg 198504, Russia
[2]Space Research Institute, Austrian Academy of Sciences, Graz 8042, Austria
[3]Laboratory for Atmospheric and Space Physics (LASP), University of Colorado Boulder, Boulder, Colorado 80303, USA
[4]Department of Mathematics, KU Leuven, Leuven B-3001, Belgium
[5]KTH Royal Institute of Technology, Stockholm SE-100 44, Sweden

[a)]andrey.div@gmail.com

ABSTRACT

We study inflow density dependence of substructures within electron diffusion region (EDR) of collisionless symmetric magnetic reconnection. We perform a set of 2.5D particle-in-cell simulations which start from a Harris current layer with a uniform background density n_b. A scan of n_b ranging from $0.02\,n_0$ to $2\,n_0$ of the peak current layer density (n_0) is studied keeping other plasma parameters the same. Various quantities measuring reconnection rate, EDR spatial scales, and characteristic velocities are introduced. We analyze EDR properties during quasisteady stage when the EDR length measures saturate. Consistent with past kinetic simulations, electrons are heated parallel to the B field in the inflow region. The presence of the strong parallel anisotropy acts twofold: (1) electron pressure anisotropy drift gets important at the EDR upstream edge in addition to the $\mathbf{E}\times\mathbf{B}$ drift speed and (2) the pressure anisotropy term $-\nabla\cdot\mathbf{P}^{(e)}/(ne)$ modifies the force balance there. We find that the width of the EDR demagnetization region and EDR current are proportional to the electron inertial length $\sim d_e$ and $\sim d_e n_b^{0.22}$, respectively. Magnetic reconnection is fast with a rate of $\sim$0.1 but depends weakly on density as $\sim n_b^{-1/8}$. Such reconnection rate proxies as EDR geometrical aspect or the inflow-to-outflow electron velocity ratio are shown to have different density trends, making electric field the only reliable measure of the reconnection rate.

I. INTRODUCTION

Magnetic reconnection is a universal plasma processes[1] which is responsible for the release of the stored magnetic energy, reconfiguration of the stressed field lines, generation of fast plasma flows, and energetic particles. Magnetic reconnection is involved in energy transfer in the Earth's magnetosphere; it drives explosive events on the solar surface and disruptions in tokamaks. The process has been the subject of many theoretical and modeling studies in past decades. It is well understood now that magnetic reconnection involves processes happening on two very different scales.[2,3] The macroscale contains the entire volume of interacting magnetic flux tubes frozen into plasma. At the microscale, the Diffusion Region(s) (DR) host(s) intense currents which allow for a diffusive mechanism (or a combination of diffusive mechanisms) to break field lines.

Diffusion region is defined formally as a region close to the X-line where the frozen-in constraint $\mathbf{E}+\mathbf{V}\times\mathbf{B}=0$ breaks for the reconnecting electric field component (hereinafter denoted as E_r). The concept of diffusion region was originally developed for single-fluid MHD approach with uniform resistivity.[4,5] The theory predicts formation of thin elongated current layers where plasma is accelerated up to the Alfvén velocity V_A. The length and width and reconnection rate scale with finite resistivity. In the absence of collisional resistivity, other mechanisms like electron inertia[6–9] break the frozen-in constraint. Ion and electron components of plasma are tied to field lines and move via $\mathbf{E}\times\mathbf{B}$ drift on large MHD scales. The motion of ion and electron

components decouples from magnetic field in, ion and electron diffusion regions (IDR and EDR, respectively) localized within a few ion/electron gyroradii to the reconnection line.

Scale separation between ions and electrons makes collisionless magnetic reconnection an inherently multiscale process. The relative motion of ions and electrons generates the Hall effect, well visible inside the IDR due to electron frozen-in constraint. The Hall term does not generate reconnection electric field, but it is argued that the Hall mediated reconnection remains fast and weakly dependent on the EDR scales[7,10,11] in Hall-MHD, hybrid, and full particle simulations.[9]

Basic IDR parameters of collisionless magnetic reconnection scale with inflow density similar to Sweet-Parker model: the downstream ion velocity is proportional to the ion Alfvén velocity V_A up to a factor, and the width is proportional to the ion inertial length[12,13] $\sim d_i$. Similarly, the EDR outflow velocity scales with the electron Alfvén velocity V_{Ae}, and thickness[10,11,14] is comparable to the electron inertial length $\sim d_e$, or some typical electron thermal gyroradius[15] ρ_e, or electron bounce width[16] λ_e in some other studies. Here, V_{Ae} and other electron parameters are calculated at the EDR inflow edge which is located deep inside IDR and where the **B** field is reduced substantially. Electrons get heated anisotropically due to parallel electrostatic potential development as they advect within the inflow region.[17,18] The EDR upstream edge location depends self-consistently[19] on the electron dissipation mechanism, mass ratio m_i/m_e, and plasma β (here plasma β is the ratio of plasma to magnetic pressure far in the inflow region).

The fluid electron momentum equation describes the electron motion in collisionless plasma

$$\mathbf{E}+\mathbf{V}^{(e)}\times\mathbf{B}=-\frac{1}{ne}\nabla\cdot\mathbf{P}^{(e)}-\frac{m_e}{e}\left(\frac{\partial\mathbf{V}^{(e)}}{\partial t}+\mathbf{V}^{(e)}\cdot\nabla\mathbf{V}^{(e)}\right). \quad (1)$$

The terms at the right-hand side of Eq. (1) are the electron pressure $-\nabla\cdot\mathbf{P}^{(e)}/(ne)$ and the inertial terms $(\partial\mathbf{V}^{(e)}/\partial t+\mathbf{V}^{(e)}\cdot\nabla\mathbf{V}^{(e)})$. In laminar symmetric case, the X-line is also the in-plane flow stagnation point making the $-\nabla\cdot\mathbf{P}^{(e)}/(ne)$ term to play a dominant role there and compensate for the E_r. The off diagonal nongyrotropic components of the electron pressure tensor $\mathbf{P}^{(e)}$ are produced by the presence of a population of electrons accelerated by E_r close to the X-line, superimposed with colder inflowing gyrotropic population.[20–23] Various models of collisionless dissipation are constructed to date involving dissipation based on laminar electron pressure inside the EDR,[14,20,24] electron viscous heat flux,[25] and anomalous turbulent processes.[26,27]

2.5D Particle-in-Cell (PIC) studies of collisionless reconnection in large ($\gg 100\,d_i$) domains found that the length of the $\mathbf{E}+\mathbf{V}_e\times\mathbf{B}\neq 0$ layer as well as the length of the fast electron jets grows with time at nearly constant width correlated with the reconnection rate decrease.[28] Generation of secondary plasmoids temporarily increased the reconnection rate due to shortening of the EDR. These results were complemented by studies of the Ohm's law terms distribution within the region where electrons are demagnetized.[29–32] A primary finding of those studies was that close to the X-line the $-\nabla\cdot\mathbf{P}^{(e)}/(ne)$ term and E_r are of the same sign as in a normal diffusion region, but the $-\nabla\cdot\mathbf{P}^{(e)}/(ne)$ term changes its sign in the outer parts, thus driving the super-Alfvénic electron jet. The origin of these outer jets was later identified to be the electron anisotropy in the EDR inflow,[18] which supports the electron momentum balance inside the EDR and controls its length. In the presence of the Hall (out-of-plane) magnetic field at the EDR edges, this gives rise to strong nongyrotropy within such outflow jets.[24]

Most simulations of collisionless magnetic reconnection were performed using Geospace Environmental Modeling (GEM) challenge setup[9] which is a plain Harris equilibrium of width 0.5–1.0 d_i, background plasma β of 0.2–0.4, and plasma density of $n_b = 0.1$–$0.2\,n_0$, the latter representing the peak plasma density in Harris current sheet. Conceptually, for such a setup $d_e \sim \rho_e$ up to a factor of 1 which implies that the effects of the electron finite-Larmor-radius (FLR, $\sim\rho_e$) are strong compared to the electron inertia effects ($\sim d_e$). Such parameters are typical for the Earth's magnetotail, but in many environments of interest the upstream plasma is much different from that. In this paper, we study properties of EDR of antiparallel collisionless symmetric magnetic reconnection with a ion-to-electron mass ratio of $m_i/m_e = 256$ and initial ion-to-electron temperature ratio of $T_i/T_e = 5$ and a set of background densities $0.02 < n_b/n_0 < 2$. We investigate the density dependence of basic EDR parameters and the microscopic reconnection rate. We aim at figuring out how far length scales and velocities deviate from the reference EDR values (d_e and V_{Ae}, respectively) for various n_b. However, establishing macroscale MHD effects or predicting self-consistent global reconnection rate is out of the scope of our paper.

Evolution of reconnection exhausts and energy exchange is connected to electron-scale processes which determine the EDR physics. Hence, much of the efforts are put into studying collisionless electron dynamics inside reconnecting thin current layers. The magnetospheric multiscale (MMS) campaign, which provides multispacecraft high-resolution measurements, is the first mission capable of detecting key features of electron-scale thin current sheets in the Earth's magnetosphere. Theoretical and numerical modeling of such dynamical plasmas is important for adequate detection and interpretation of diffusion regions and electron outflow jet crossings in spacecraft data,[22] and for better understanding of microphysics of the process.

The primary aim of our study is to investigate different substructures formed inside the EDR and study density dependence. Therefore, considerable effort is spent discussing formal definitions of EDR spatial scales and other characteristic quantities. The paper is organized as follows: Section II contains a brief description of the simulation code used and parameters employed. Section III presents the reference run with background density of 0.1 similar to GEM-challenge studies and discusses various EDR length measures (inner EDR, outer EDR, remagnetization region, Sec. III A) based on the Ohm's law terms balance. Temporal evolution of the length measures and reconnection electric field is studied in Secs. III B and III C, respectively, to select specific times when the process is quasisteady. Section IV presents a systematic density dependence study: width measures (Sec. IV A), length (Sec. IV B), reconnection electric field and upstream microscopic B field (Sec. IV C), and velocities (Sec. IV D). Finally, Sec. V presents conclusions and discussion.

II. PIC SIMULATIONS AND NORMALIZATION

We solve the 2.5D magnetic reconnection problem numerically using the semi-implicit Particle-in-Cell (PIC) code[33] iPIC3D in which implicit moment method[34] is implemented. The code iPIC3D was utilized previously in application to such problems as magnetic reconnection studies,[14,35,36] reconnection jet fronts,[37–40] and other studies.[41,42] The code is capable of using realistic ion-to-electron mass ratio

m_i/m_e, but a fixed ratio of $m_i/m_e = 256$ is used in the present paper to reduce computational costs. The key feature of the implicit moment method is to use closure equations to approximate the feedback from current and plasma density in Maxwell's equations over a computational cycle from time t to time $t + dt$. In contrast to full-implicit PIC schemes (where equations for a time step $t + dt$ contain unknown fields and particles of the time layer $t + dt$), the closure equations allow to calculate the field sources removing the need to implicitly solve for particles at the time step $t + dt$. Hence, second-order implicit equation for electric field at the time step $\mathbf{E}(t + dt)$ appears, containing plasma moments (density, currents, and pressure) at time step t.

The simulation setup is similar to that of past studies of undriven magnetic reconnection. To summarize: The initial condition is provided by two conventional Harris sheets[43] within a double-periodic computational domain. Magnetic field is

$$B_x(y) = B_0(\tanh((y - L_y/4)/\lambda_H) - \tanh((y - 3L_y/4)/\lambda_H) - 1)$$

and the density profile is

$$n^{(s)}(y) = n_0(\cosh^{-2}((y - L_y/4)/\lambda_H) + \cosh^{-2}((y - 3L_y/4)/\lambda_H)) + n_b^{(s)}.$$

The current sheet half-width $\lambda_H = 0.5\ d_i$ and s denotes ions ($s = i$) and electrons ($s = e$). The uniform background density is $n_b = 2$, 1, 0.5, 0.3, 0.1, 0.04, 0.03, 0.02 (runs R1–R8, respectively). The x axis is parallel to the initial magnetic field, the z axis is parallel to the initial Harris sheet current, and the y axis completes the right-hand system.

Density is normalized to the peak Harris current sheet density n_0, and the magnetic fields are normalized to the asymptotic value B_0. Lengths are expressed in units of ion inertial length $d_i = c/\omega_{pi}$, where ω_{pi} is the ion plasma frequency based on n_0. Time is expressed in units of inverse ion cyclotron frequency $\Omega_{ci} = eB_0/(m_i c)$ based on B_0, and velocities are normalized to the Alfvén velocity based on B_0 and n_0.

Ion-to-electron temperature ratio is $T^{(i)}/T^{(e)} = 5$ for both background and current sheet populations in all runs. Initial thermal velocities of electron and ion populations are, respectively, $c/u_{the} = 22.2$, $c/u_{thi} = 159$. Alfvén velocity computed for n_0 and B_0 is $c/V_A = 103$ in all runs. Local Alfvén velocities V_{Al} computed for each run for B_0 and n_b can be found in Table I. The computational domain is a two-dimensional box with the dimensions $L_x \times L_y$, a uniform grid $N_x \times N_y$, and grid spacing $\Delta x = \Delta y = L_x/N_x = L_y/N_y$. A localized X-point perturbation is added to start reconnection at the point $(L_x/2, L_y/4)$. The instantaneous main X-line position (x^*, y^*) is determined as a saddle point location[44] with a minimum of $|B|$ closest to $(L_x/2, L_y/4)$. The drift velocity of (x^*, y^*) is much smaller than typical velocities of electrons inside the EDR and hence does not affect the scaling study. Other parameters (including time step $dt\Omega_{ci}$ and number of initial macroparticles N_{Pcell} per cell per species) are listed in Table I:

III. SIMULATION OVERVIEW FOR $N_b = 0.1$

A. EDR structure and length measures

In this section, we present an overview of a simulation ($n_b = 0.1$, run R5) developing under the parameters similar to the ones found in the GEM magnetic reconnection challenge.[9]

A common pattern of single X-line collisionless reconnection is displayed in Fig. 1 for times $t = 21.728$ (leftmost panels) and $t = 33.95$ (rightmost panels). Figures 1(a)–1(i) show, respectively, the Ohm's law terms, electron velocity components, the two-dimensional structure of $V_y^{(e)}$, electron pressure anisotropy $\log_{10}P_\parallel^{(e)}/P_\perp^{(e)}$, off diagonal component $P_{yz}^{(e)}$, gyrotropic part of $P_{yz}^{(e)G}$, a rotated component[24] $\tilde{P}_{yz}^{(e)}$, nongyrotropy measure[45] $\sqrt{Q^{(e)}}$, and electron frame dissipation measure[46] D_e'. The gyrotropic part of the pressure tensor is denoted usually as $\mathbf{P}^G = P_\perp\mathbf{I} + (P_\parallel - P_\perp)\mathbf{bb}$, where $P_\parallel = \mathbf{bPb}$ and $P_\perp = (Tr(\mathbf{P}) - P_\parallel)/2$ are, respectively, the electron pressure components parallel and perpendicular to the local magnetic field direction given by $\mathbf{b} = \mathbf{B}/|\mathbf{B}|$.

EDR is subdivided into different parts depending on the balance between generalized Ohm's law terms.[29,31] In agreement with previous studies (e.g., Refs. 12, 16, 47, and 48), the electron nongyrotropy $P_{yz}^{(e)} - P_{yz}^{(e)G}$ supports E_z at the X-line and hosts a load region ($D_e' > 0$) in the innermost EDR part (bounded by red lines in Fig. 1). The velocity $V_x^{(e)}$ peaks downstream of this region (marked by green lines, Fig. 1), where the electron pressure component in the Ohm's law $(-\nabla \cdot \mathbf{P}^{(e)})_z/(ne)$ reverses due to strong gyrotropic parallel anisotropy $P_\parallel^{(e)} \gg P_\perp^{(e)}$ existing in the EDR inflow and hence producing a gyrotropic contribution[24] to $P_{yz}^{(e)G}$. A rotated component $\tilde{P}_{yz}^{(e)}$ (cast in a coordinate system aligned with the electron flow and from which the upstream anisotropy is subtracted) is nearly uniform throughout this region.[24] Thus, an electron jet with $|[\mathbf{V}^{(e)} \times \mathbf{B}]_z| > |E_z|$ forms outside of the inner EDR. Whether this region between blue lines in Fig. 1 is a "true" EDR[28,29,49] or not[14,30,31,50] is yet a matter of debate. In what follows, we use a conventional "definition":[30,51]

TABLE I. Summary of simulations R1–R8 parameters. The initial upstream electron beta[19] is $\beta_{e\infty} = n_b T_e/(B_0^2/2)$.

Run	n_b/n_0	$L_x \times L_y$	$N_x \times N_y$	Δ_x	$\beta_{e\infty}$	$dt\Omega_{ci}/10^{-3}$	N_{Pcell}	c/V_{Al}
R1	2.0	$61.44d_i \times 28.8d_i$	3072×1440	0.02	0.333	0.67	100	145.8
R2	1.0	$61.44d_i \times 28.8d_i$	3072×1440	0.02	0.1667	0.67	100	103.1
R3	0.5	$96d_i \times 24d_i$	3456×864	0.0278	0.0833	0.78	140	72.9
R4	0.3	$76.8d_i \times 36d_i$	3072×1440	0.025	0.05	0.67	144	56.5
R5	0.1	$192d_i \times 60d_i$	4608×1440	0.0417	0.01667	0.67	80	32.6
R6	0.04	$144d_i \times 72d_i$	1728×864	0.0833	0.00667	0.87	80	20.6
R7	0.03	$192d_i \times 96d_i$	2304×1152	0.0833	0.005	0.87	100	17.8
R8	0.02	$165.9d_i \times 77.76d_i$	3072×1440	0.054	0.00167	1.0	100	14.6

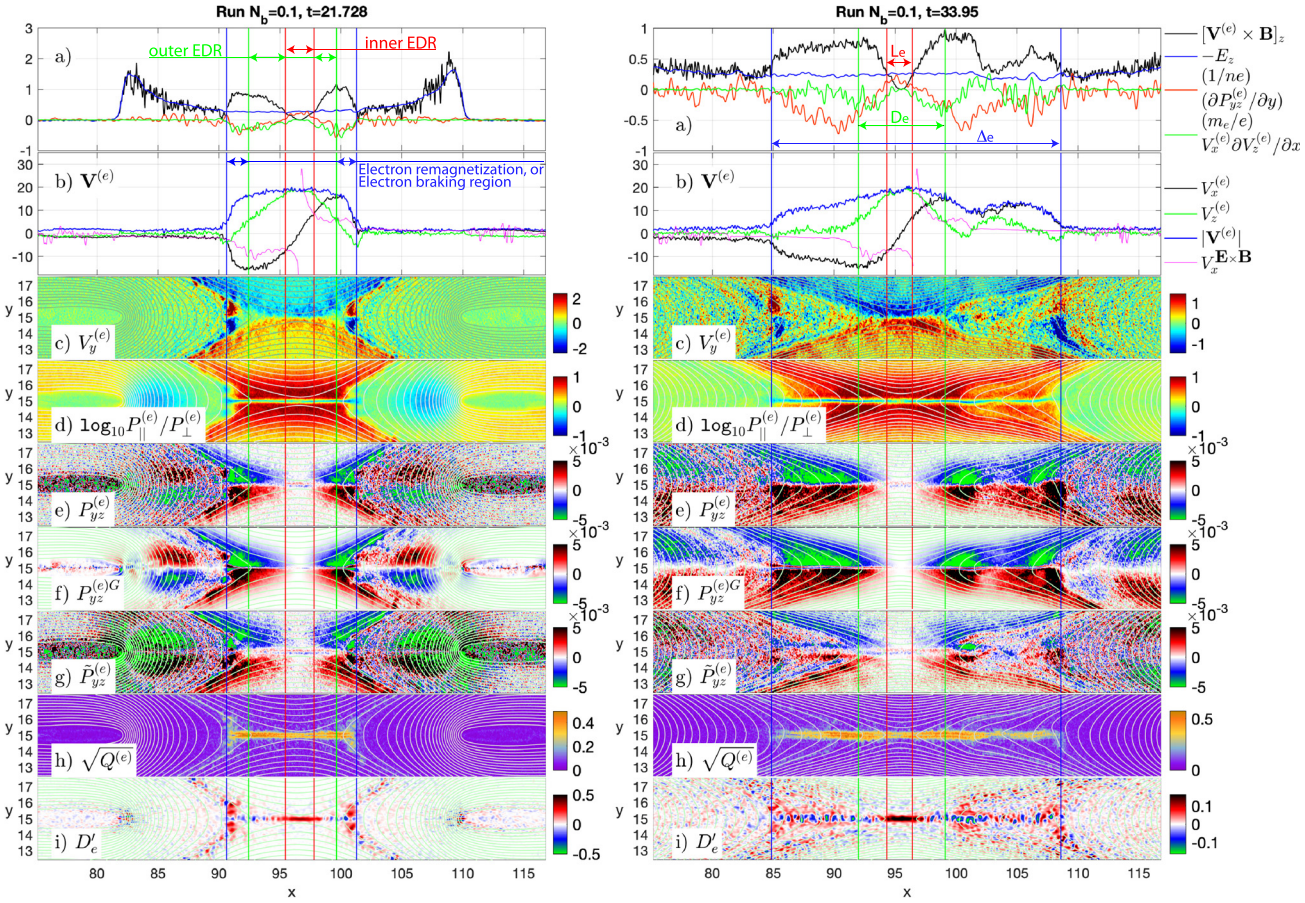

FIG. 1. (a) Ohm's law terms. (b) Electron velocities and the x component of the $\mathbf{E}\times\mathbf{B}$ drift speed ($V_x^{\mathbf{E}\times\mathbf{B}}$). (c) $V_y^{(e)}$. (d) $\log_{10}P_{\parallel}^{(e)}/P_{\perp}^{(e)}$. (e) $P_{yz}^{(e)}$. (f) Gyrotropic part of $P_{yz}^{(e)}$, given by $P_{yz}^{(e)G}=(P_{\perp}^{(e)}\mathbf{I}+(P_{\parallel}^{(e)}-P_{\perp}^{(e)})\mathbf{bb})_{yz}$, where $\mathbf{b}=\mathbf{B}/|\mathbf{B}|$ is the magnetic field direction. (g) Rotated component[24] $\tilde{P}_{yz}^{(e)}$. (h) Electron nongyrotropy measure[45] $\sqrt{Q^{(e)}}$. (i) Electron dissipation measure[46] D'_e. Plots are shown for two selected time slices, before ($t=21.728$) and after ($t=33.95$) the quasi-steady EDR regime is reached. Definitions of inner EDR, outer EDR, and electron braking (remagnetization) region are shown in left panels. Length measures L_e, D_e, and Δ_e are shown in right panels.

- Red lines in Fig. 1 mark the extent of the inner EDR based on the condition[14,30,50] $E_z+[\mathbf{V}^{(e)}\times\mathbf{B}]_z=0$ at $y=y^*$. We denote the distance between those points as $2L_e$. Typically, electron velocity there is $\sim 1/3$ of its peak exhaust value.[14,52]
- Green lines mark points where $|V_x^{(e)}|$ peaks in the outflow direction (approximately corresponds to the overshoot of $|E_z+[\mathbf{V}^{(e)}\times\mathbf{B}]_z|$). We define the distance between those points as $2D_e$.
- Blue lines are plotted for points where electrons are remagnetized and thus $E_z+[\mathbf{V}^{(e)}\times\mathbf{B}]_z=0$ marking the full length of electron demagnetization region. We denote the distance between those points[29] as $2\Delta_e$.

Electrons slow down in a region downstream of the outer EDR [Fig. 1(g)], inside the Electron Remagnetization Jet (ERJ) or electron braking region. The electron remagnetization jet starts to open downstream of the outer EDR. This region is also denoted as outer layer or outflow jet,[29] or super-Alfvénic electron jet,[31] or E^2DR (Extended Electron Diffusion Region).[53] There, the electron flow slows down to match the $\mathbf{E}\times\mathbf{B}$ drift velocity[51,54] (shown by blue lines in Fig. 1). Remagnetization causes pitch angle mixing of accelerated particles,[55] gyrotropization, and heating due to betatron effect.[19,55] The remagnetization jet is likely formed by accelerated meandering particles superimposed on a population of inflowing electrons that follow noncrossing Speiser orbits which dominate outside the inner and outer EDRs.[54] The substructures within the full electron demagnetization region continue to evolve after $t=21.768$ (Fig. 1, left panels) so the quasisteady stage is reached later. By the time $t=33.95$ (Fig. 1, right panels), the region of large $\sqrt{Q^{(e)}}$ elongates considerably as well as the D'_e region. Such configuration appears to be similar to dissipation-less electron current layer.[56] At such later times, there is no electron remagnetization shock[57] standing at the outflow EDR edge, which now contains an elongated electron braking region.

B. Temporal evolution of EDR extent

Time evolution of l_e, L_e, D_e, Δ_e for run R5, $n_b=0.1$ is displayed in Fig. 2. Here, l_e is the EDR width based on the Ohm's law violation scale, which is half the distance between the points $E_z+[\mathbf{V}^{(e)}\times\mathbf{B}]_z=0$ along the line $x=x^*$. Times $t=21.73$ and $t=33.94$ (shown by black lines) are moments displayed in Fig. 1. The structure of the EDR continues to evolve until quasisteady stage is reached. The growth of

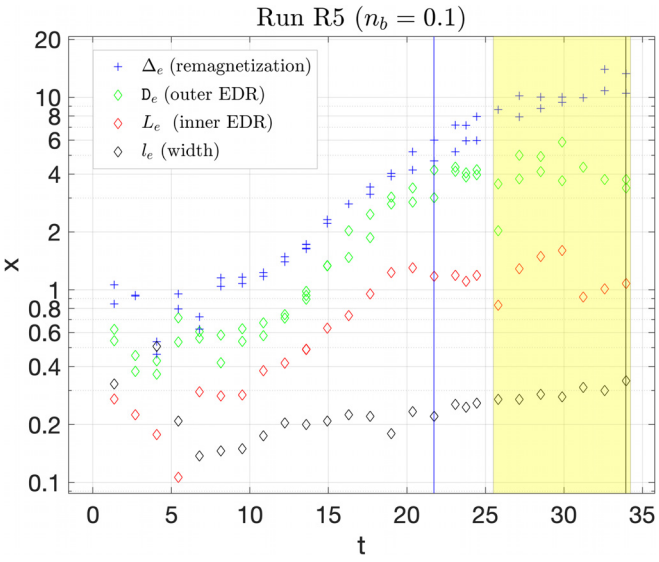

FIG. 2. EDR scales (width and lengths) evolution for run R5 ($n_b = 0.1$). Vertical lines mark time slices selected to plot Fig. 1. Yellow rectangle marks times when data for density dependence study are sampled with run R5.

L_e saturates by $t \sim 18$, followed by D_e saturation at $t \sim 22$ and finally Δ_e stops growing by $t > 25$. Notably, the computational domain measures $L_x \times L_y = 192d_i \times 36d_i$ in run R5; hence, periodic boundary conditions (BCs) do not impede electron demagnetization region stretching. The EDR width l_e grows weakly likely because of magnetic flux and density depletion but remains close to $l_e \sim 0.3$ by $25 < t < 30$. A time interval marked yellow represents the run R5 times for which single X-line EDR parameters are sampled for density scaling analysis. For each run, we select an interval matching the following criteria: (1) Δ_e growth saturates implying that L_e and D_e are also steady, (2) there are no large-scale plasmoids which introduce large asymmetry in reconnection outflows, and (3) reconnection outflows are not affected by periodic BCs. We need to point out that due to limited computational resources we do not consider very long reconnection evolution (hundreds of Ω_{ci}^{-1}), which is perturbed by regular plasmoid formation[52,53] leading to fluctuations in reconnection rate and EDR parameters. The question as to how plasmoid formation impacts reconnection rate and heating globally has long been discussed in literature[19,28,37,53,58] but seems to be open at present.

C. Time evolution of reconnection rates

The un-normalized electric field E_z in the X-line [Fig. 3(a)] is presented in code units. In much similarity with other reconnection studies,[13,48,53] an overshoot in E_z is formed at early stage of the evolution, when the Harris sheet is reconnected. The overshoot is more noticeable for smaller background densities since the reconnection electric field scales with the Alfvén upstream velocity $V_A^{(up)} \sim n_b^{-1/2}$. Random fluctuations are due to PIC noise or generation of small-scale flux ropes (more visible for smaller densities in runs R7 and R8); hence, we select several times (marked in Fig. 3 for each run) at quasisteady stage for the detailed EDR study. Long time simulations with duration exceeding $\sim 300\Omega_{ci}^{-1}$ in fully open systems[52,53] display periodic formation of magnetic islands near the diffusion region, leading to large variations in EDR scales. Comparing Fig. 3(a) (run R5 curve) and Fig. 2, one observes that the time of peak reconnection rate (time $t \sim 17$) is a transient stage before the scales L_e, D_e, Δ_e saturates. Hence, it is possible that EDR scaling relations produced for such a peculiar moment of time[59] significantly deviate from typical parameters in quasisteady regime.

The microscopic ion rate of conversion of stored magnetic energy (the normalized reconnection rate) is conventionally measured as a dimensionless ratio of the plasma inflow speed V toward the diffusion

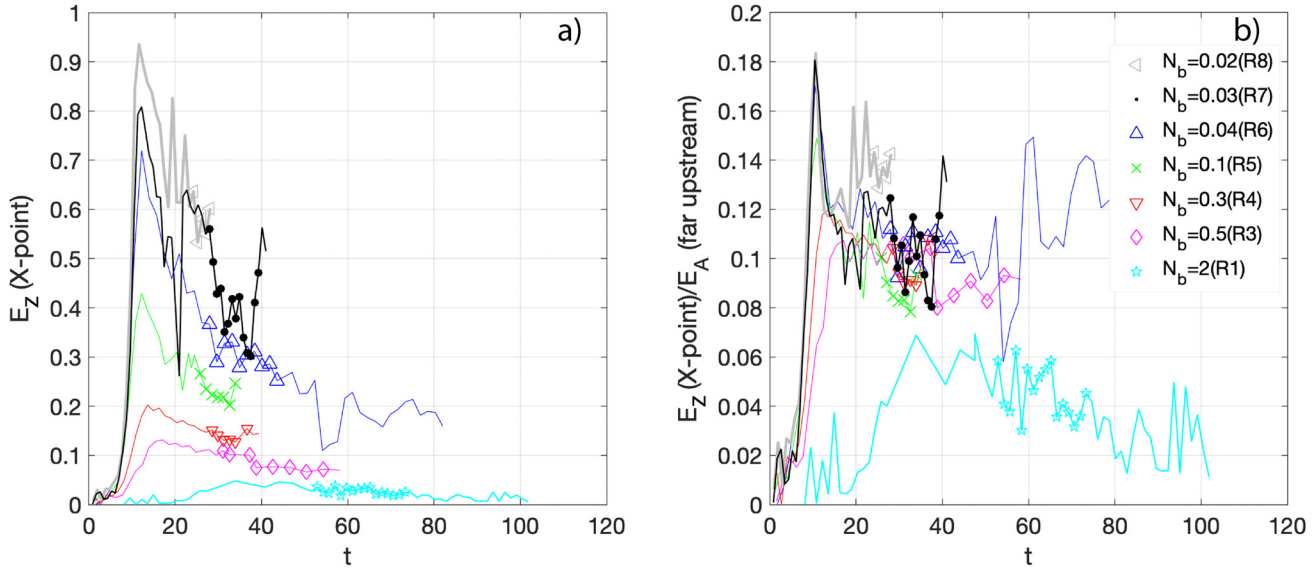

FIG. 3. (a) Un-normalized reconnection rate (electric field E_z at the main X-line). (b) Microscopic ion reconnection rate $\varepsilon_r = E_z/E_A^{(up)}$, for all runs. In each line, the symbols mark moments chosen for quasi-steady study.

region and the ion Alfvén velocity $V_A^{(up)}$ upstream: $\varepsilon_r = V/V_A^{(up)}$, or equivalently $\varepsilon_r = E_z/E_A^{(up)}$, where the upstream Alfvén electric field is $E_A^{(up)} = B^{(up)} V_A^{(up)}$. We estimate parameters $B^{(up)}$ and $V_A^{(up)}$ at a point $y = 2d_i(n_b)$ to the X-line[19] ($d_i(n_b)$ based on the local density at the X-line), which approximately represents the IDR upstream edge. Figure 3(b) shows ε_r vs time for each run. As a first check we find the microscopic ion reconnection rate to be $\varepsilon_r \sim 0.1$, in agreement with other studies.[9]

IV. EDR DENSITY DEPENDENCE STUDY

In this section, we study systematically the n_b dependence of characteristic EDR velocities, spatial scales, and reconnection rate.

The quantitative comparison of the EDR parameters requires knowledge of the typical **B** field and density at the upstream edge because the electron Alfvén velocity and electron inertial length are, respectively, the typical velocity and width scale. It is found in simulations[19] that the density inside EDR is very close to $n^{(up)}$ for the range of plasma β studied. To reduce noise, we average the plasma density in a box $|x - x^*| < L_e$, $|y - y^*| < d_e(n_b)/2$. Unlike density, the magnetic field $|B_x(x^*, y)|$ increases monotonically with $|y - y^*|$ from 0 within the diffusion region; therefore, the magnetic field and characteristic velocity V_{Ae} (see Sec. IV C) depend on a specific definition of width (see Sec. IV A) in a given set of simulation data.

A. Structure scales around the neutral line

Let us examine quantitatively spatial profiles of various common measures used for identifying the electron diffusion region structure. Below we define formally several width measures commonly used as a proxy of EDR thickness.

- l_e: The scale of the Ohm's law violation identified rigorously as half the distance between the points $E_z + [\mathbf{V}^{(e)} \times \mathbf{B}]_z = 0$ along the line $x = x^*$ [see Figs. 4(a1) and 4(a2)].
- l_{je}: The half-thickness of the electron current layer defined as a distance from the X-line to a point where $j_z^{(e)}$ is half of its maximum value at $x = x^*$ profile inside the EDR [see Figs. 4(c1) and 4(c2)]. Note that we sample magnetic field $B_x^{(2je)}$ at a point[13] $(x^*, y^* + 2l_{je})$ since the point $(x^*, y^* + l_{je})$ is inside the EDR.

Other physical scales measured are as follows:

- l_D: The thickness of the electron-frame dissipation measure[46] (D_e' layer). $l_{\mathbf{J}\cdot\mathbf{E}}$: same as the latter, but for the quantity $\mathbf{J}\cdot\mathbf{E}$ layer. l_{JzEz}:

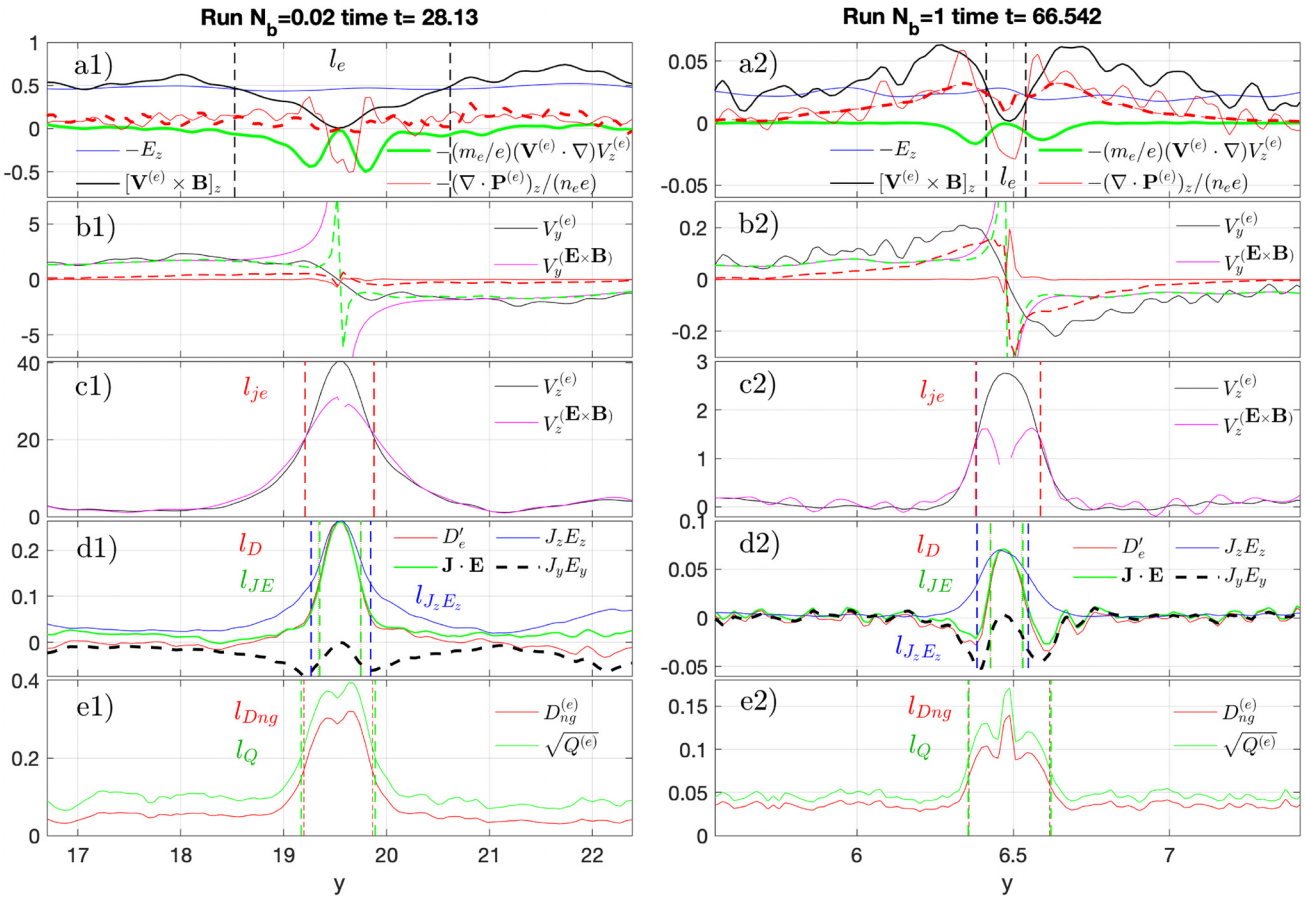

FIG. 4. In this figure, we show qualitative differences between the low- and high-density cases. Vertical cuts through the X-line $x = x^*$ of the Ohm's law terms and velocities. Definitions of various width measures of an EDR (see details in Sec. IV A).

same as the latter, but for the quantity J_zE_z layer. Figures 4(d1) and 4(d2) show the respective dissipation measures (D'_e, $\mathbf{J}\cdot\mathbf{E}$, $J_z\cdot E_z$) along a cut through $x = x^*$.

- l_{Dng}: The thickness of the nongyrotropic electron layer[60] D_{ng}. l_Q: same as the latter, but for electron nongyrotropy measure[45] $\sqrt{Q^{(e)}}$. Figures 4(e1) and 4(e2) show the respective nongyrotropy measures (D_{ng}, $\sqrt{Q^{(e)}}$) along a cut through $x = x^*$.
- ρ_e: The electron meandering orbit amplitude evaluated as a point where the local electron gyroradius equals the distance to the X-line $|y - y^*|$ at $x = x^*$.

Figure 5 shows how the discussed quantities (l_e, l_{je}, l_D, $l_{J\cdot E}$, $l_{J_zE_z}$, l_{Dng}, l_Q, ρ_e) vary with n_b. Quantities are normalized by the local electron inertial length $d_e(n^{(up)})$ to remove the general trend $\sim d_e \sim n_b^{-1/2}$.

The following important conclusions could be made. First, the measured quantities are proportional to the local d_e with a coefficient approximated by a power law $\propto n_b$ (alternatively, $\propto \beta_{e\infty}$). To ease comparison of noisy data, we plot regression lines and power law indices for each set of measured quantities. Second, the resulting slope of $l_e/d_e \sim n_b^{-0.03}$ is nearly zero which agrees well with other studies[11,61] performed using both kinetic and two-fluid approaches. The Ohm's law violation scale l_e is governed by fluid Hall electron dynamics[12,14] producing the scaling $l_e \sim d_e$. Also (see Sec. IV C), the $B_x^{(l_e)}$ field calculated at the upstream EDR edge $y - y^* = l_e$, $x = x^*$ appears nearly constant for the studied range of β_e. It should be noted that this result is at odds with the adiabatic equations of state which set the EDR edge according to the electron firehose condition[18,19] (see Appendix A). Third, other scales introduced in Fig. 5 have nonzero slopes with power law indices close to 0.2. Notably, the characteristic thickness of the nongyrotropic layer l_{Dng} is slightly larger than the electron meandering width ρ_e in agreement[60,62] with studies of the EDR

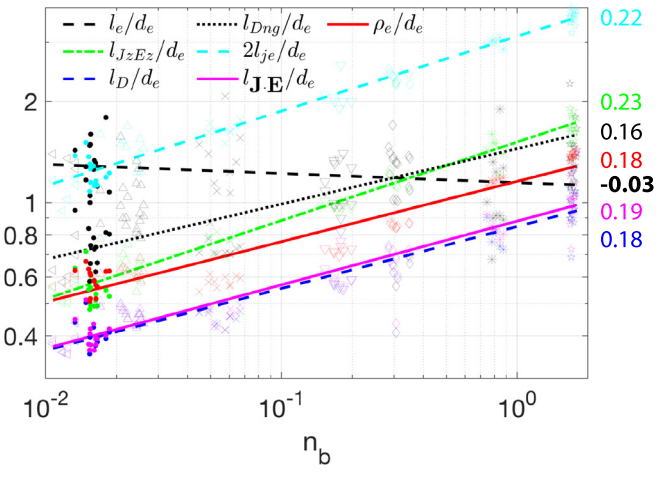

FIG. 5. Density dependence of various width measures. All quantities are normalized by the local electron inertial length $d_e(n^{(up)})$ to remove the general trend $\sim d_e \sim n_b^{-1/2}$. Single points represent the EDR widths sampled at specific times when magnetic reconnection is in the steady state regime (the specific times are emphasized in Fig. 3 with large markers). Respective power law fits are shown with numbers, e.g., $l_e/d_e \sim n_b^{-0.03}$ is nearly independent of n_b but other width measures scale as approximately $2l_{je}/d_e \sim n_b^{-0.22}$.

signatures. To summarize, the Ohm's law violation scale and the EDR current width are governed by "different" physical mechanisms.

Let us examine qualitatively the discrepancy between l_e and l_{je} scales. We revisit the Ohm's law terms in Figs. 4(a1) and 4(a2) along a vertical cut through $x = x^*$ for $n_b = 0.02$ and $n_b = 1$, respectively. Right at the X-point, both runs display common results: the terms $[\mathbf{V}^{(e)}\times\mathbf{B}]_z \sim 0$ and $-(m_e/e)(\mathbf{V}^{(e)}\cdot\nabla\mathbf{V}^{(e)})_z \sim 0$; the nongyrotropic pressure component $(-\nabla\cdot\mathbf{P}^{(e)})_z/(ne)$ balances E_z, and the latter is uniform in the diffusion region vicinity. The differences are visible close to the EDR edges and further upstream. The inertial term (which reduces to $-(m_e/e)V_y^{(e)}\partial_y V_z^{(e)}$ at $x = x^*$) appears because the current velocity gradient $\partial_y V_z^{(e)}$ is large at the inflow edge [see Fig. 4(c)]. Hence, one presumes the spatial scale of the inertial term extent is proportional to the EDR current layer width l_{je} and the sign is $-(m_e/e)V_y^{(e)}\partial_y V_z^{(e)} < 0$. The pressure term profile is composed of two different regions: one inside the EDR $(-\nabla\cdot\mathbf{P}^{(e)})_z/(ne) < 0$ (originated from the electron-meandering motion with a spatial extent proportional to ρ_e), and the other in the inflow region formed by adiabatically trapped electrons and providing[18,19] $(-\nabla\cdot\mathbf{P}^{(e)G})_z/(ne) > 0$ with $P_\parallel^{(e)} > P_\perp^{(e)}$. The gyrotropic contribution $\mathbf{P}^{(e)G}$ is shown with a dashed red line in Figs. 4(a1) and 4(a2).

The profiles in Figs. 4(a1) and 4(a2) reveal qualitative differences between low and high density cases.

For $n_b = 0.02$ case (run R8), the inertial contribution clearly exceeds the pressure term contribution at $|y - y^*| = l_{je}$. The overshoot is $(-\nabla\cdot\mathbf{P}^{(e)})_z/(ne) > 0$ with a partial counterbalance existing between those two terms. This effect appears in the interval $d_e < |y - y^*| < l_e$ in low-beta plasma as FLR effect[49] and is typically interpreted as gyroviscous cancelation.[12] The sum is

$$(-\nabla\cdot\mathbf{P}^{(e)})_z/(ne) - (m_e/e)V_y^{(e)}\partial_y V_z^{(e)} < 0$$

at $|y - y^*| = l_{je}$; hence, the convective term satisfies $|[\mathbf{V}^{(e)}\times\mathbf{B}]_z| < |E_z|$ and a point $|y - y^*| = l_e$ is pushed at a larger distance to the X-line than l_{je}. The gyrotropic part $\mathbf{P}^{(e)G}$ is relatively low.

In $n_b = 1.0$ case (run R2), the electron pressure term strongly exceeds $|E_z|$ at the EDR upstream edge due to substantial contribution from gyrotropic part $\mathbf{P}^{(e)G}$ existing in the inflow region. We suggest that the $(-\nabla\cdot\mathbf{P}^{(e)})_z/(ne)$ term should play a major role at $|y - y^*| = l_{je}$ in high β plasmas, and there is no gyroviscous cancelation in such a regime. The sum of dissipative terms is

$$(-\nabla\cdot\mathbf{P}^{(e)})_z/(ne) - (m_e/e)V_y^{(e)}\partial_y V_z^{(e)} > 0,$$

hence $|[\mathbf{V}^{(e)}\times\mathbf{B}]_z| > |E_z|$. The point $|y - y^*| = l_e$ shifts closer to the X-line and is embedded within the dissipative electron layer [cf. the scales defined in Fig. 4(e2)].

Next we discuss how the nonideal electric fields change the velocity of electrons flowing into the EDR. The classical Sweet-Parker-like diffusion region analysis presumes that the dissipative electric field peaks at the DR center and drops monotonically with distance to the X-line at the DR edges. Accordingly, the convective electric field converges to the reconnection electric field to satisfy the frozen-in condition, making the scale of the Ohm's law violation (l_e) proportional to the dissipative current sheet width (l_{je}). PIC simulations reveal that extra nondissipative terms come into play at the EDR edges; therefore,

one expects the $[\mathbf{V}^{(e)} \times \mathbf{B}]_z$ profile to compensate for the contribution of the inertial and pressure components since the reconnection electric field is uniform in the quasisteady phase. To understand the effects controlling the inflow of electrons into the EDR, we show $V_y^{(e)}$ along the y direction in Figs. 4(b1) and 4(b2) show. We plot the $\mathbf{E} \times \mathbf{B}$ drift velocity (magenta) and the "modified[49] $\mathbf{E} \times \mathbf{B}$ drift velocity"

$$V_y^{(\mathbf{E}\times\mathbf{B})'} = E_z/\left(B_x - (m_e/e)\partial V_z^e/\partial y\right),$$

which accounts for the large $-(m_e/e)V_y^{(e)}\partial_y V_z^{(e)}$ contribution [Fig. 4(a1)] for $n_b = 0.02$ case. Additional electron drifts are caused by the gyrotropic pressure gradient and field line curvature in the inflow region[63]

$$\begin{aligned}\mathbf{V}_{\perp dia}^{(e)} &= -\frac{1}{enB^2}\mathbf{B}\times\nabla\cdot\mathbf{P}^{(e)}\\ &= -\frac{1}{enB^2}\mathbf{B}\times\nabla p_\perp - \frac{1}{enB^2}\left(P_\parallel^{(e)} - P_\perp^{(e)}\right)\mathbf{B}\times((\mathbf{b}\cdot\nabla)\mathbf{b}).\end{aligned}$$

The solid red line expresses the profile of the diamagnetic drift $-(1/enB^2)\mathbf{B}\times\nabla p_\perp$. The dashed red line represents the pressure anisotropy drift. In agreement with a previous study,[49] the modified $\mathbf{E}\times\mathbf{B}$ drift velocity follows closely the velocity $V_y^{(e)}$ for $n_b = 0.02$, and diamagnetic drift is close to zero in such a case. Opposite to latter, the $n_b = 1.0$ case reveals that $V_y^{(e)}$ strongly exceeds $V_y^{\mathbf{E}\times\mathbf{B}}$ drift because of pressure anisotropy drift (red dashed line), with the diamagnetic drift velocity being close to zero (red solid line) in the inflow region. Hence, the $\mathbf{E}\times\mathbf{B}$ drift velocity does "not" necessarily represent the inflow velocity of electrons, which must have important implications for reconnection rate estimate and Sweet-Parker analysis of EDR.

B. EDR length scales

Let us study the EDR dimensions in the X direction. We found that there are different ways to define lengths (L_e, D_e, Δ_e discussed in Sec. III A) and widths (l_e, l_{je} discussed in Sec. IV A). We measure different length estimates for all runs and plot the results in Fig. 6(a) in code units. Figures 6(b) and 6(c) display these estimates normalized to local d_e and $2l_{je}$, respectively. To guide the eye, we plot regression lines and power law indices for each set.

Figure 6(a) reveals that power law fits are very close to $-1/2$ and hence scale with electron inertial length $d_e \sim n_b^{-1/2}$. Subtracting this general trend, one observes several striking features in Fig. 6(b): (1) regression lines for L_e/d_e, D_e/d_e and Δ_e/d_e roughly lie on a straight line and hence are nearly independent of density ($\sim n_b^{-0.03}\ldots n_b^{-0.05}$). (2) The EDR aspect ratios l_e/L_e, l_e/D_e depend very weakly on density, pointing[3] to a reconnection rate on the order of 0.1 which is independent of n_b as well (also see Sec. IV C).

According to common scaling analyses based on conservation laws,[14,15] the width scales well with d_e and the EDR width-to-length ratio is identical to the electron reconnection rate ε_e up to a coefficient.[52] A recent scaling analysis[59] provides corrections to this scheme. A weak power law scales for $l_e \sim 2d_e\beta_e^{1/8}$ [Eq. (6) of Ref. 59] and $L_e \sim 3\beta_e^{1/4}(d_i d_e)^{1/2}$ [Eq. (11) of Ref. 59] were found. For a fixed electron to ion mass ratio and a fixed initial temperature, these equations provide $l_e \sim 2d_e n_b^{1/8}$ and $L_e \sim 3n_b^{1/4}d_e$, respectively, giving the inner EDR aspect ratio $L_e/l_e \sim n_b^{1/8}$, which is clearly at odds with our Fig. 6(b).

We suggest that the analysis performed in Ref. 59 reflects the correct upstream T_e dependence but is only valid for a limited upstream n_b range ($0.2 < n_b < 0.5$) and reconnection rate peak time. The electron behavior is fully kinetic inside the EDR, but the Ohm's law demagnetization scales (l_e, L_e) behave conceptually the same as in fluid simulations since it is argued that the EDR scales are independent of the mechanism which breaks the frozen-in condition.[11,64] Next we plot the regression lines in Fig. 6(c) (length estimates scaled to $2l_{je}$) and find a substantial trend ($\sim n_b^{-0.26\cdots-0.34}$). In fact, such a trend agrees well with density dependence of $2l_{je}/l_e \sim n_b^{0.22}$ discussed in Sec. IV A (see Fig. 5). An intriguing property of l_{je} scale is that for high n_b case the aspect ratio $2l_{je}/L_e$ approaches unity which clearly contradicts a common scaling analyses[3] predicting reconnection rates on the order of $\sim 0.1 - 0.2$. As discussed in Sec. IV A, non-$\mathbf{E}\times\mathbf{B}$ drifts are capable of modifying the EDR inflow velocity. Hence, electron pressure anisotropy drift pushes plasma into the EDR making the reconnection rate

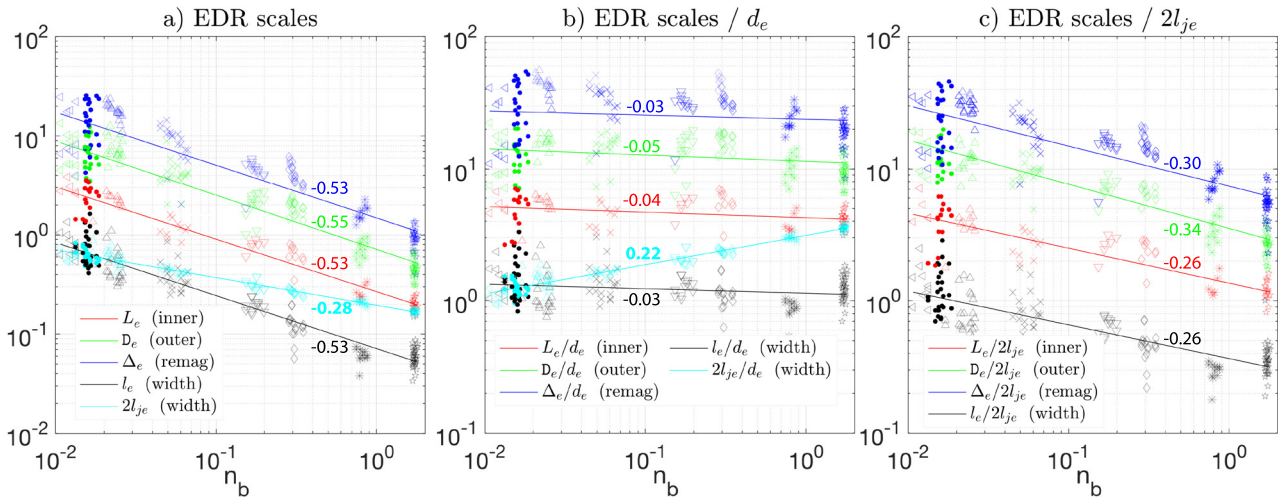

FIG. 6. EDR Length measures for all runs: (a) un-normalized. (b) Lengths $/d_e$. (c) Lengths $/2l_{je}$. Respective power law fits are shown with numbers.

ε_r very different from the geometrical aspect ratio. We discuss this point next.

C. Reconnection electric field and upstream $B^{(up)}$ field

To compare quantitatively electron outflow velocities, one needs to introduce typical electron Alfvén velocities and upstream EDR magnetic fields first.

The estimates for the upstream EDR edge magnetic field B_x are $B_x^{(l_e)}$, $B_x^{(je)}$, and $B_x^{(2je)}$ computed at $x = x^*$ and $y = y^* - l_e$, $y = y^* - l_{je}$ $y = y^* - 2l_{je}$, respectively. The EDR edge field $B_x^{(l_e)}$ defined at the frozen-in condition violation width appears nearly constant [black dashed line in Fig. 7(a)] with $B_x^{(l_e)} \sim n_b^{-0.01}$. Quantities defined by electron current width scale l_{je} show a clear trend with n_b which agrees relatively well with the analytical scaling[18] plotted by red line (also see Appendix A). The theory is known to break down[19] for $\beta_{e\infty} < 0.03$ (which corresponds to $n_b = 0.18$ for initial conditions considered) causing ~1.5 times underestimate in our low n_b runs. The overall scaling for $0.02 < n_b < 2$ is $B_x^{(2je)} \sim n_b^{1/8}$, but more exact theory is needed to couple self-consistently[65] the microscale EDR properties and macroscale global plasma flow.

Magnetic field $B^{(up)}$ upstream of the X-line is plotted with a gray line in Fig. 7(a). Notably, $B^{(up)}$ is nearly independent of density ($\sim n_b^{0.01}$). The scaling study in Ref. 13 reported the trend $0.55 < B^{(up)} < 0.7$ for $0.01 < n_b < 1$. We attest such difference with our results to the system size and periodic boundary conditions dependence or the low mass ratio $m_i/m_e = 25$ in Ref. 13 causing the ion-scale physics to "feel" heavy electrons.

The density dependence of the un-normalized reconnection rate E_r (which equals electric field $|E_z|$ in the X-line in code units) is presented in Fig. 7(b). The electric field depends monotonically for approximately an order of magnitude with a power law index of $\sim n_b^{-0.62}$ which is close to the Alfvén velocity dependence $\sim n_b^{-1/2}$. We calculate the upstream Alfvén electric field $E_A^{(up)} \sim n_b^{-0.46}$ [gray line in Fig. 7(b)] to estimate the microscopic ion reconnection rate ε_r for all runs. The microscopic inner electron reconnection rate $\varepsilon_e = E_z/E_{Ae}^{(l_e)}$ is represented in units of electron Alfvén electric field[14,32] $E_{Ae}^{(l_e)} = B_x^{(l_e)} V_{Ae}^{(l_e)} \sim n_b^{-0.51}$ [black line in Fig. 7(b)] where $V_{Ae}^{(l_e)}$ is the electron Alfvén velocity based on $B_x^{(l_e)}$. The red line in Fig. 7(b) shows the analytical estimate[18] of the electron Alfvén electric field at the EDR edge using the same magnetic field shown in Fig. 7(a) with the red dotted line.

A power law regression for $E_A^{(up)} \sim n_b^{-0.46}$ follows closely $E_z \sim n_b^{-0.62}$, but in fact the normalized outer reconnection rate $\varepsilon_r = E_z/E_A^{(up)}$ is not really a constant although being close[9] to ~0.1 [Fig. 7(c)]. The line of regression [Fig. 7(c), gray line] shows a weak scaling of $\varepsilon_r \sim n_b^{-0.13}$ in agreement with other studies[13,19] which reported fading of the normalized ε_r as density increases. As a consistency check, for "standard" GEM-like conditions, the line of regression of $\varepsilon_r(n_b)$ crosses $\varepsilon_r = 0.1$ at $n_b \sim 0.1$. A steeper trend is found for $E_r/E_{Ae}^{(2je)} \sim n_b^{-0.39}$ [Fig. 7(c), cyan line] where $E_{Ae}^{(2je)} = B_x^{(2je)} V_{Ae}^{(2je)} \sim n_b^{-0.23}$ is based on magnetic field $B_x^{(2je)}$ which grows twofold in the interval $0.01 < n_b < 2$.

D. Velocities

Electron jet outflow velocity is known to scale as the electron Alfvén velocity[10,11,65] which implies $\sim n_b^{-1/2}$ dependence. Figure 8(a) shows density dependence of the outflow ($V_x^{(e)}$) velocities measured within the region of electron demagnetization:

- $V_{xL}^{(e)}$ at the inner EDR edge ($y = y^*$, $x = x^* - L_e$), plotted with the red solid line;
- $V_{xD}^{(e)}$ at the outer EDR edge ($y = y^*$, $x = x^* - D_e$), plotted with the green solid line;
- $V_{x\Delta}^{(e)}$ at the outer EDR edge ($y = y^*$, $x = x^* - \Delta_e$), plotted with the blue solid line.

In addition to that, we plot the following reference EDR velocities in Fig. 8(a):

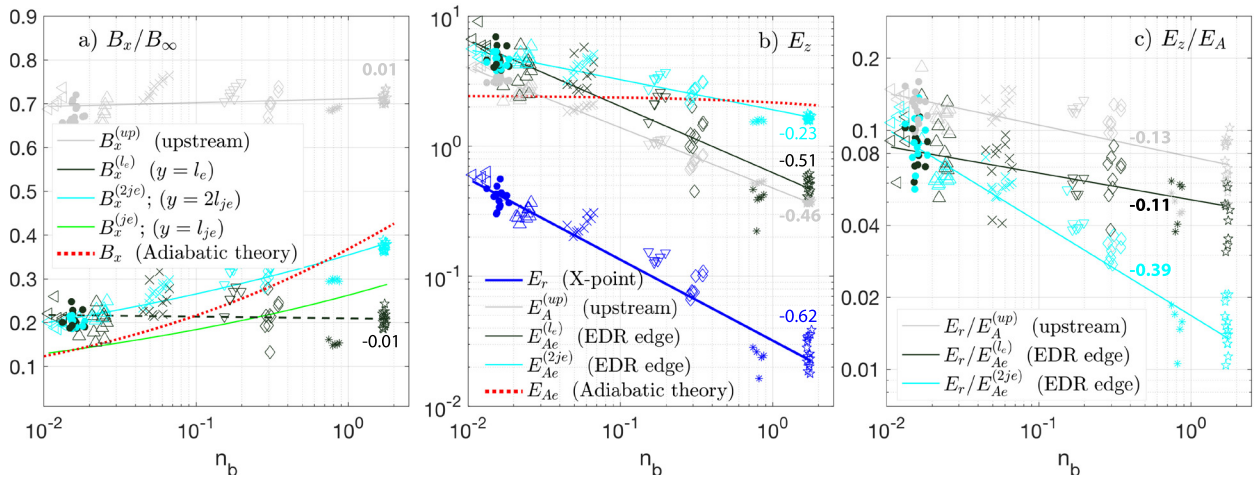

FIG. 7. (a) Magnetic field measured at the far inflow and upstream of the EDR. (b) Un-normalized reconnection rate for all runs; E_A at the far inflow and E_{Ae} upstream of the EDR for all runs. (c) Reconnection rate as normalized to $E_A^{(up)}$ (microscopic ion), $E_{Ae}^{(l_e)}$ (microscopic electron), $E_{Ae}^{(2je)}$. Respective power law fits are shown with numbers.

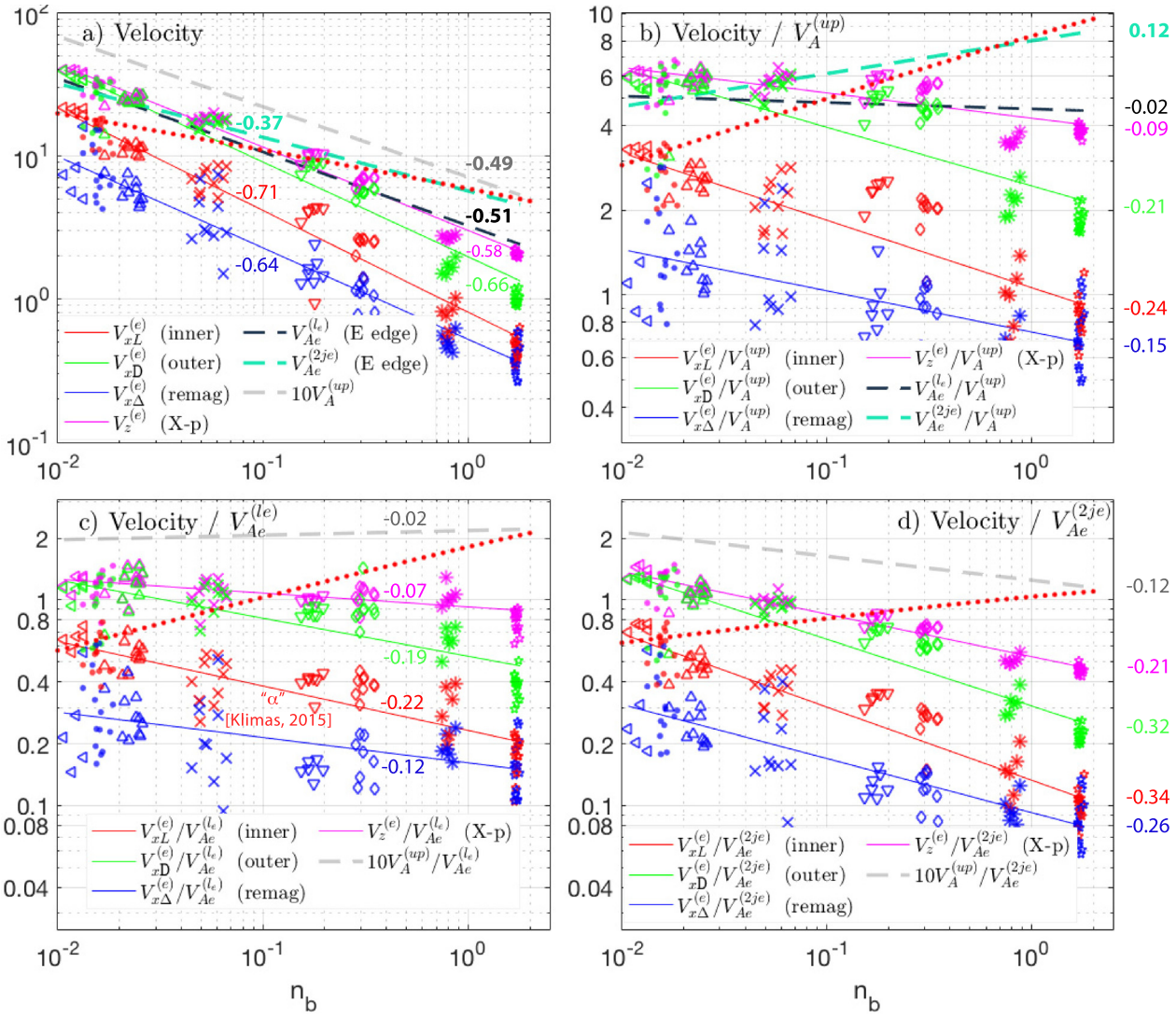

FIG. 8. Characteristic EDR velocities combined for all runs: (a) un-normalized. (b) Velocities $/V_A^{(up)}$. (c) Velocities $/V_{Ae}^{(l_e)}$. Notably, the ratio $V_{xL}^{(e)}/V_{Ae}^{(l_e)}$ is denoted[52] as α and has a significant trend with density, $\alpha \sim n_b^{-0.22}$. (d) Velocities/$V_{Ae}^{(2je)}$. Respective power law fits are shown with numbers.

- electron Alfvén velocity based on the upstream EDR edge magnetic field which is computed using adiabatic theory[18] and stability condition

$$\left(P_{\parallel}^{(e)}(n,B) - P_{\perp}^{(e)}(n,B)\right)/B^2 = 1$$

shown by the red dotted line. Notably, the adiabatic theory estimate is rather different from other quantities since accelerating potential is comparable or exceeds the upstream electron temperature[18] for low n_b limit. See details in Appendix A.
- Electron Alfvén velocity $V_{Ae}^{(l_e)}$ based on $B_x^{(l_e)}$ at $y - y^* = l_e$ (black dashed line);
- electron Alfvén velocity $V_{Ae}^{(2je)}$ based on $B_x^{(2je)}$ at $y - y^* = 2l_{je}$ (green dashed line);
- electron current velocity $V_z^{(e)}$ computed right at the X-line ($y = y^*$, $x = x^*$, magenta solid line);
- ion Alfvén velocity $V_A^{(up)}$ based on **B** at far inflow, see Fig. 7(a) (gray solid line).

Lines of regression for the reference EDR velocities $V_A^{(up)} \sim n_b^{-0.49}$ and $V_{Ae}^{(up)} \sim n_b^{-0.51}$ display power law trends very close to $\sim n_b^{-1/2}$ [Fig. 8(a)]. Hence, we resolve the usual Alfvén speed dependence for these quantities. Unlike $B_x^{(up)} \sim n_b^{0.01}$ and $B_x^{(l_e)} \sim n_b^{-0.01}$, the magnetic field $B_x^{(2je)}$ (determined by the current width at $y - y^* = 2l_{je}$) increases with n_b, leading to a flatter $V_A^{(2je)} \sim n_b^{-0.37}$ dependence. With magnetic field $B_x^{(2je)}$ being close to that provided by the adiabatic theory [Fig. 7(a)], the corresponding analytical electron Alfvén velocity is close to $V_{Ae}^{(2je)}$.

Lines of regression for the current velocity $V_z^{(e)}$ and EDR exhaust velocities display steeper dependence with n_b. Trends are presented with greater details in Figs. 8(b) and 8(c) which display velocities normalized by, respectively, $V_A^{(up)}$, $V_{Ae}^{(le)}$, $V_{Ae}^{(2je)}$.

The current velocity $V_z^{(e)}$ normalized to $V_{Ae}^{(l_e)}$ has almost no n_b dependence on $V_z^{(e)}/V_{Ae}^{(l_e)} \sim n_b^{-0.07}$. Since the current velocity $V_z^{(e)}$ supports the EDR magnetic field reversal and $B_x^{(l_e)}/l_e = -neV_z^{(e)}$, one estimates for the typical EDR thickness ($l_e = d_e$): $V_z^{(e)} = V_{Ae}^{(l_e)}$. The Hall reconnection model states that the whistler wave controls the outflow of electrons from the X-line. The Hall field produced by the x-directed stream of electrons is equal to $B_x^{(l_e)}$; hence, the equality $V_{x\mathrm{D}}^{(e)} = V_z^{(e)}$ should be satisfied at the EDR outflow edge. However, the peak exhaust velocity $V_{x\mathrm{D}}^{(e)}$ is close to $V_z^{(e)}$ for GEM-challenge like parameters and more generally for $n_b < 0.2$. For the highest density run R1, the ratio $V_z^{(e)}/V_{x\mathrm{D}}^{(e)}$ is ~ 2 [Fig. 8(a)]; hence, the current and exhaust velocities are not necessarily identical in the Hall reconnection model.

One notices the ordering of the exhaust velocities: $V_{x\Delta}^{(e)} < V_{xL}^{(e)} < V_{x\mathrm{D}}^{(e)}$. The velocity $V_{x\Delta}^{(e)}$ is sampled at the outflow edge of the remagnetization region where electrons start to $\mathbf{E}\times\mathbf{B}$ drift with a speed proportional to the local "ion" Alfvén velocity $V_A^{(up)}$ [seen well at Fig. 8(b)]. The peak exhaust velocity $V_{x\mathrm{D}}^{(e)}$ is reached in the outer EDR, where $|[\mathbf{V}^{(e)}\times\mathbf{B}]_z| > |E_z|$. The line of regression is $V_{x\mathrm{D}}^{(e)}/V_{Ae}^{(l_e)} \sim n_b^{-0.19}$; hence, the ratio falls with n_b which conforms a past study[19] of density dependence. Regression lines of $V_{x\Delta}^{(e)} \sim n_b^{-0.64}$, $V_{xL}^{(e)} \sim n_b^{-0.71}$, $V_{x\mathrm{D}}^{(e)} \sim n_b^{-0.66}$, $V_z^{(e)} \sim n_b^{-0.58}$ are very close suggesting that the EDR substructures are qualitatively similar for all runs studied.

The inner EDR exhaust velocity $V_{xL}^{(e)}$ reaches neither $V_{Ae}^{(l_e)}$ nor $V_{Ae}^{(2je)}$ [Figs. 8(c) and 8(d)] in agreement with past scaling studies[14,52] because of the strong electron anisotropy at the inflow region and the corresponding "blocking" effect.[24,30] The ratio $V_{xL}^{(e)}/V_{Ae}^{(l_e)} \sim n_b^{-0.22}$ was denoted by α in Ref. 52 and was considered to be a universal constant independent of the m_i/m_e ratio, density, and temperature. The value of $\alpha = 0.45$ was obtained for $n_b = 0.2$ but smaller ion-to-electron mass ratios ($m_i/m_e = 25, 100$) during a series of very long GEM-challenge like runs with open boundaries.[52] Our study provides a similar value of $\alpha = 0.33$ at $n_b = 0.2$ [Fig. 8(c)] using the regression line for $V_{xL}^{(e)}/V_{Ae}^{(l_e)}$.

For $0.02 < n_b < 2.0$, the power law fit displays a range of $0.6 > \alpha > 0.2$, making the effectiveness of the electron acceleration strongly density-dependent. We qualitatively explain this trend via the Alfvénic relation[31] for the outflow velocity, $V_x^{(e)} = V_{Ae}d_e/l_{je}$, which is based on mass conservation. Comparing the power law fit of $d_e/l_{je} \sim n_b^{-0.22}$ (Fig. 4) to results of our study in Figs. 8(c) and 8(d), one indeed finds a close agreement with $V_{xL}^{(e)}/V_{Ae}^{(l_e)} \sim n_b^{-0.22}$ and $V_{xL}^{(e)}/V_{Ae}^{(2je)} \sim n_b^{-0.34}$. If all the available magnetic energy at the EDR inflow edge $\sim(B_x^{(l_e)})^2/2$ is transformed into bulk kinetic energy, then the electron fluid should reach the electron Alfvén velocity $V_{Ae}^{(l_e)}$. Simulations indicate that for high n_b a smaller share of the available magnetic energy upstream of the EDR $(\sim B_x^{(l_e)})^2/2$ is transformed into kinetic energy at the EDR exhaust.

V. DISCUSSION AND CONCLUSIONS

In this paper, we studied density dependence of undriven symmetric magnetic reconnection using a set of 2.5D PIC simulations. The primary goal of our study was to measure various EDR properties (length scales, velocities, reconnection rate, etc.) and compare them to the characteristic quantities, namely, the electron inertial length (d_e), the electron Alfvén velocity (V_{Ae}), and electron Alfvén electric field (E_{Ae}).

In contrast to a common conclusion (based on a number of GEM-challenge like studies) that the microscopic reconnection rate is a universal *constant*[3,9] ~ 0.1 in a wide range of upstream parameters, our study shows that the ion $(E_z/E_A^{(up)})$ and inner electron $(E_z/E_{Ae}^{(l_e)})$ reconnection rate estimates depend on $\sim n_b^{-1/8}$.

In order to further pinpoint differences between various reconnection rate measures, we revisit a simplistic Sweet-Parker-like analysis.[14,28] The EDR is approximated as a box of length D and width l (without referring to whether l_e or l_{je}). For an incompressible plasma, the conservation of mass provides $n\mathrm{D}V_{yl}^{(e)} = nlV_{x\mathrm{D}}^{(e)}$. The electrons are frozen-in at inflow and outflow EDR boundaries; therefore,

$$|V_{x\mathrm{D}}^{(e)}B_y^{(\mathrm{D})}| = |V_{yl}^{(e)}B_x^{(l)}| = |E_z|. \tag{2}$$

Assuming that the outflow magnetic field $B_y^{(\mathrm{D})}$ measured at $(x = \mathrm{D}, y^*)$ is negligible $(B_y^{(\mathrm{D})} \ll B_x^{(l)})$ and the inflow magnetic energy is converted exclusively into exhaust kinetic energy (which is a rough approximation since it neglects heating), one gets the outflow velocity equal to the electron Alfvén velocity computed for magnetic field $B_x^{(l)}$: $V_{x\mathrm{D}} = V_{Ae}^{(l)}$. Dividing Eq. (2) by $E_{Ae}^{(l)} = V_{Ae}^{(l)}B_x^{(l)}$, common Sweet-Parker-like expressions are recovered,

$$\frac{V_{yl}^{(e)}}{V_{x\mathrm{D}}^{(e)}} = \frac{B_y^{(\mathrm{D})}}{B_x^{(l)}} = \frac{l}{\mathrm{D}} = \frac{E_z}{E_{Ae}^{(l)}} \equiv \varepsilon_e. \tag{3}$$

We plot these ratios in Fig. 9. Reconnection rate measure based on aspect ratio $l_e/\mathrm{D}_e \sim n_b^{-0.01}$ is nearly a constant ~ 0.1. A measure

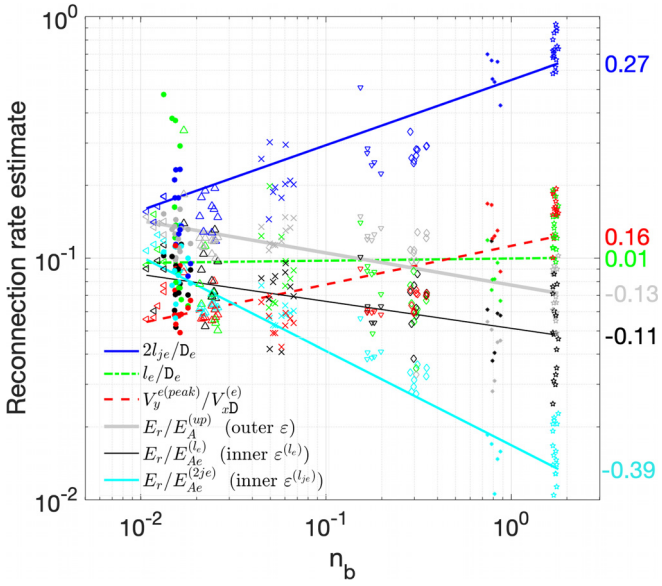

FIG. 9. Comparison of various proxies for reconnection rate: $2l_{je}/\mathrm{D}_e$, l_e/D_e, a ratio of peak inflow electron velocity to peak exhaust velocity $V_y^{e(peak)}/V_{x\mathrm{D}}^{(e)}$, reconnection electric field E_z normalized by $E_A^{(up)}$, $E_{Ae}^{(l_e)}$, $E_{Ae}^{(2je)}$.

based on velocities $V_y^{e(peak)}/V_{xD}^{(e)} \sim n_b^{0.16}$ equals 0.1 for $n_b = 0.3$. The measure $l_{je}/D_e \sim n_b^{0.27}$ displays a strong trend with density since $2l_{je}/d_e \sim n_b^{0.22}$.

The ratios presented in Eq. (3) are not identical and display different trends with density. We hypothesize (but do not prove here) that similar trends might exist with respect to temperature and/or m_i/m_e ratio; hence, the study of antiparallel symmetric reconnection is far from being fully solved from a theoretical perspective. The ultimate rate of magnetic field conversion is provided "only" by electric field which is noisy due to waves and instabilities and other instrumental uncertainties in observations and is known to be a tricky quantity to measure in experiment.

We recapitulate our results:

(1) The microscopic electron reconnection rate measure weakly decreases with density, $\varepsilon_e = E_r/E_{Ae}^{(l_e)} \sim n_b^{-0.11}$. A similar trend appears for the microscopic ion reconnection rate measure $\varepsilon_r = E_r/E_A^{(up)} \sim n_b^{-0.13}$. The value of $\varepsilon_r = 0.1$ is found at GEM-challenge like parameters for $n_b \sim 0.2$. Flow reconnection rate, EDR, aspect ratio, and ε_e are different.
(2) Ohm's law study along a cut through the EDR ($x = x^*$) in Sec. IV A allows us to conclude that it is the presence of a non-$\mathbf{E} \times \mathbf{B}$ drift at the inflow EDR edge which makes the reconnection rate estimates based on electron velocity or electric field that different. The electron component and the $\mathbf{B}$ field are detached so as the field reconnection rate and flow reconnection rate.
(3) A point where $V_x^{(e)}$ peaks ($x - x^* = D_e$, the outer EDR exhaust edge) should be considered the EDR outflow edge even though electron component is not frozen-in there due to upstream pressure anisotropy.
(4) The inner EDR outflow velocity $V_{xL}^{(e)}$ is denoted as[52] α when normalized by $V_{Ae}^{(l_e)}$: $\alpha \sim n_b^{-0.22}$ and not a universal constant as was suggested.
(5) EDR spatial measures normalized to the electron inertial length, L_e/d_e, D_e/d_e, and Δ_e/d_e are nearly independent of density.
(6) Geometrical and fluid properties of the EDR are subject to of density dependence which are not in agreement with estimates provided by Ref. 59. The time of the reconnection rate peak used for performing the scaling study by Ref. 59 does not contain the fully developed EDR (inner and outer parts) and electron remagnetization jet. We summarize our findings in Appendix B.

ACKNOWLEDGMENTS

This research was supported by the Russian Science Foundation (RNF No. 18-47-05001). D.K. was supported by Austrian Science Fund (FWF) No. I 3506-N27. A.D. thanks M. Sitnov and S. Merkin for fruitful discussions. The simulations were conducted on the resources of KTH, Stockholm (Sweden, Project Nos. m.2017-1-390 and 2017-1-422) and MSU at Lomonosov supercomputing facility Project Nos. 1576 and 1658, Moscow (Russia). Access to simulation data can be provided upon request.

APPENDIX A: ADIABATIC ELECTRON PRESSURE CLOSURE EQUATIONS

We revisit below the electron pressure closure equations used to approximate the B field at the EDR upstream edge [Fig. 7(a), red dashed line] and corresponding electron Alfvén velocity (Fig. 8, red dashed lines). A theory of adiabatic electron acceleration during collisionless reconnection developed by Egedal[17,18,66] states that electron pressure is not isotropic close to the EDR. Resulting electron distribution functions show strong parallel anisotropy[66] reaching $P_\parallel^{(e)}/P_\perp^{(e)} \sim 6$ or even[24] $P_\parallel^{(e)}/P_\perp^{(e)} \sim 10$. The theory assumes the presence of a parallel electric field potential which traps electrons with initially low parallel velocity $V_\parallel^{(e)}$ (trapped population) near the X-line. Another population of passing (accelerated) electrons crosses the x line vicinity in a single shoot and produces an isothermal Boltzmann-like response in the distribution function.

Two invariants are conserved (namely, the magnetic moment μ and parallel action integral, $J = \int V_\parallel dl$, where integration is performed between turning points[67]) as a magnetized particle moves through the reconnection inflow. This allows constructing an approximate solution of the Vlasov equation upstream of the EDR and also derivation of the fluid closure for $P_\parallel^{(e)}$ and $P_\perp^{(e)}$

$$\tilde{P}_\parallel^{(e)} = F(a/2)\tilde{n} + F(a^{-1}/2)\frac{\pi\tilde{n}^3}{6\tilde{B}^2}, \tag{A1}$$

$$\tilde{P}_\perp^{(e)} = F(a)\tilde{n} + F(a^{-1})\tilde{n}\tilde{B}, \tag{A2}$$

where quantities are normalized to the values upstream of the reconnection ("source") region: $\tilde{n} = n/n^{(up)}$ (we neglect density variation in our calculations, hence $\tilde{n} \sim 1$); $\tilde{B} = B/B^{(up)}$, $\tilde{P}^{(e)} = P^{(e)}/P^{(up)}$, $a = \tilde{n}^3/\tilde{B}^2$, $F(a) = (1+a)^{-1}$. The expressions (A1) and (A2) provide closed equations of state[67] $P_\parallel^{(e)}(n,B)$, $P_\perp^{(e)}(n,B)$. Next, the model assumes that the EDR upstream edge is controlled by the firehose instability threshold and the solution of

$$\left(P_\parallel^{(e)}(n,B) - P_\perp^{(e)}(n,B)\right)/B^2 = 1$$

provides the EDR edge magnetic field.

We use the approximation (A1) and (A2) to estimate the $\mathbf{B}$ field and the corresponding electron Alfvén velocity V_{Ae} at the EDR edge

- Figure 7(a) (red dotted line) shows the EDR edge magnetic field provided by the adiabatic theory. The solution agrees relatively well with the value computed at the electron current layer thickness (l_{je}) for $n_b < 1$. The adiabatic solution strongly overestimates the EDR $\mathbf{B}$ field for larger n_b's.
- Figure 7(b) (red dotted line) shows the electron Alfvén electric field computed for the adiabatic $\mathbf{B}$ value.
- Figure 8(a) (red dotted line) shows the electron Alfvén velocity in code units; Figs. 8(b)–8(d) show the electron Alfvén velocity normalized by, respectively, Alfvén velocity far upstream $V_A^{(up)}$, $V_{Ae}^{(le)}$ and $V_{Ae}^{(2je)}$.

APPENDIX B: SUMMARY OF POWER LAW REGRESSION FITS

Summary of power law regression fits is presented in Table II.

TABLE II. Summary of simulations R1–R8 parameters.

Quantity	Fits	Nakamura[59]
$B_x^{(up)}$	$\sim const\ (n_b^{0.01})$	
$B_x^{(l_e)}$	$\sim const\ (n_b^{-0.01})$	
L_e	$\sim d_e n_b^{-0.04}$	$\sim \beta^{1/4}(d_i d_e)^{1/2}$

TABLE II. (*Continued.*)

Quantity	Fits	Nakamura[59]
l_e	$\sim d_e n_b^{-0.03}$	$\sim \beta_e^{1/8} d_e$
l_{Dng}	$\sim d_e n_b^{0.16}$	$\sim 3\beta_e^{3/8}\sqrt{1+0.15\beta_e^{-1/2}}\,d_e$
		$\sim n_b^{0.28}$ (our parameters)
l_{je}	$\sim d_e n_b^{0.22}$	
ε_e	$\sim n_b^{-0.11}$	
ε_r	$\sim n_b^{-0.13}$	
$\alpha = V_{xL}^{(e)}/V_{Ae}^{(l_e)}$	$\sim n_b^{-0.22}$	$\sim const$ Ref. 52
$V_z^{(e)}/V_{Ae}^{(l_e)}$	$\sim n_b^{-0.07}$	

REFERENCES

[1]E. R. Priest and T. Forbes, *Magnetic Reconnection: MHD Theory and Applications* (Cambridge University Press, 2000), p. 600.
[2]H. E. Petschek, NASA Spec. Publ. **50**, 425 (1964); available at http://adsabs.harvard.edu/abs/1964NASSP..50..425P).
[3]Y.-H. Liu, M. Hesse, F. Guo, W. Daughton, H. Li, P. Cassak, and M. Shay, Phys. Rev. Lett. **118**, 085101 (2017).
[4]E. N. Parker, ApJS **8**, 177 (1963).
[5]P. Sweet, Il Nuovo Cimento (1955–1965) **8**, 188 (1958).
[6]V. M. Vasyliunas, Rev. Geophys. **13**, 303, https://doi.org/10.1029/RG013i001p00303 (1975).
[7]M. E. Mandt, R. E. Denton, and J. F. Drake, Geophys. Res. Lett. **21**, 73, https://doi.org/10.1029/93GL03382 (1994).
[8]M. A. Shay and J. F. Drake, Geophys. Res. Lett. **25**, 3759, https://doi.org/10.1029/1998GL900036 (1998).
[9]J. Birn, J. F. Drake, M. A. Shay, B. N. Rogers, R. E. Denton, M. Hesse, M. Kuznetsova, Z. W. Ma, A. Bhattacharjee, A. Otto, and P. L. Pritchett, J. Geophys. Res. **106**, 3715, https://doi.org/10.1029/1999JA900449 (2001).
[10]D. Biskamp, E. Schwarz, and J. F. Drake, Phys. Rev. Lett. **75**, 3850 (1995).
[11]M. A. Shay, J. F. Drake, B. N. Rogers, and R. E. Denton, J. Geophys. Res. **106**, 3759, https://doi.org/10.1029/1999JA001007 (2001).
[12]A. Ishizawa and R. Horiuchi, Phys. Rev. Lett. **95**, 045003 (2005).
[13]P. Wu, M. A. Shay, T. D. Phan, M. Oieroset, and M. Oka, Phys. Plasmas **18**, 111204 (2011).
[14]A. Divin, G. Lapenta, S. Markidis, V. S. Semenov, N. V. Erkaev, D. B. Korovinskiy, and H. K. Biernat, J. Geophys. Res. (Space Phys.) **117**, A06217, https://doi.org/10.1029/2011JA017464 (2012).
[15]D. Tsiklauri, Phys. Plasmas **15**, 112903 (2008); e-print arXiv:0808.0143.
[16]M. M. Kuznetsova, M. Hesse, and D. Winske, J. Geophys. Res. **103**, 199, https://doi.org/10.1029/97JA02699 (1998).
[17]J. Egedal, W. Fox, N. Katz, M. Porkolab, M. Øieroset, R. Lin, W. Daughton, and J. Drake, J. Geophys. Res.: Space Phys. **113**, A12207, https://doi.org/10.1029/2008JA013520 (2008).
[18]A. Le, J. Egedal, W. Fox, N. Katz, A. Vrublevskis, W. Daughton, and J. Drake, Phys. Plasmas **17**, 055703 (2010).
[19]A. Le, J. Egedal, and W. Daughton, Phys. Plasmas **23**, 102109 (2016); e-print arXiv:1609.09508 [physics.plasm-ph].
[20]K. Fujimoto and R. D. Sydora, Phys. Plasmas **16**, 112309 (2009).
[21]A. Divin, S. Markidis, G. Lapenta, V. S. Semenov, N. V. Erkaev, and H. K. Biernat, Phys. Plasmas **17**, 122102 (2010).
[22]M. Hesse, T. Neukirch, K. Schindler, M. Kuznetsova, and S. Zenitani, Space Sci. Rev. **160**, 3 (2011).
[23]J. Ng, J. Egedal, A. Le, W. Daughton, and L.-J. Chen, Phys. Rev. Lett. **106**, 065002 (2011).
[24]A. Divin, V. Semenov, D. Korovinskiy, S. Markidis, J. Deca, V. Olshevsky, and G. Lapenta, Geophys. Res. Lett. **43**, 10565, https://doi.org/10.1002/2016GL070763 (2016).
[25]M. Hesse, M. Kuznetsova, and J. Birn, Phys. Plasmas **11**, 5387 (2004).
[26]J. F. Drake, M. Swisdak, C. Cattell, M. A. Shay, B. N. Rogers, and A. Zeiler, Science **299**, 873 (2003).
[27]W. Daughton, V. Roytershteyn, H. Karimabadi, L. Yin, B. J. Albright, B. Bergen, and K. J. Bowers, Nature **7**, 539 (2011); available at https://www.nature.com/articles/nphys1965.
[28]W. Daughton, J. Scudder, and H. Karimabadi, Phys. Plasmas **13**, 072101 (2006).
[29]H. Karimabadi, W. Daughton, and J. Scudder, Geophys. Res. Lett. **34**, L13104, https://doi.org/10.1029/2007GL030306 (2007).
[30]M. A. Shay, J. F. Drake, and M. Swisdak, Phys. Rev. Lett. **99**, 155002 (2007). 0704.0818.
[31]J. F. Drake, M. A. Shay, and M. Swisdak, Phys. Plasmas **15**, 042306 (2008).
[32]A. Klimas, M. Hesse, and S. Zenitani, Phys. Plasmas **15**, 082102 (2008).
[33]S. Markidis, G. Lapenta *et al.*, Math. Comput. Simul. **80**, 1509 (2010).
[34]J. U. Brackbill and D. W. Forslund, J. Comput. Phys. **46**, 271 (1982).
[35]G. Lapenta, S. Markidis, A. Divin, M. Goldman, and D. Newman, Phys. Plasmas **17**, 082106 (2010).
[36]S. Markidis, P. Henri, G. Lapenta, A. V. Divin, M. V. Goldman, D. Newman, and S. Eriksson, Nonlinear Processes Geophys. **19**, 145 (2012).
[37]G. Lapenta, S. Markidis, M. V. Goldman, and D. L. Newman, Nat. Phys. **11**, 690 (2015).
[38]A. Divin, Y. V. Khotyaintsev, A. Vaivads, M. André, S. Markidis, and G. Lapenta, J. Geophys. Res.: Space Phys. **120**, 2675, https://doi.org/10.1002/2014JA020503 (2015).
[39]F. Pucci, W. H. Matthaeus, A. Chasapis, S. Servidio, L. Sorriso-Valvo, V. Olshevsky, D. L. Newman, M. V. Goldman, and G. Lapenta, ApJ **867**, 10 (2018); e-print arXiv:1810.13318 [astro-ph.SR].
[40]V. Olshevsky, S. Servidio, F. Pucci, L. Primavera, and G. Lapenta, ApJ **860**, 11 (2018).
[41]J. Deca, A. Divin, G. Lapenta, B. Lembège, S. Markidis, and M. Horányi, Phys. Rev. Lett. **112**, 151102 (2014).
[42]J. Deca, A. Divin, C. Lue, T. Ahmadi, and M. Horányi, Commun. Phys. **1**, 12 (2018).
[43]E. G. Harris, Il Nuovo Cimento (1955–1965) **23**, 115 (1962).
[44]H. Fu, A. Vaivads, Y. V. Khotyaintsev, V. Olshevsky, M. André, J. Cao, S. Huang, A. Retinò, and G. Lapenta, J. Geophys. Res.: Space Phys. **120**, 3758, https://doi.org/10.1002/2015JA021082 (2015).
[45]M. Swisdak, Geophys. Res. Lett. **43**, 43, https://doi.org/10.1002/2015GL066980 (2016); e-print arXiv:1509.00787 [physics.space-ph].
[46]S. Zenitani, M. Hesse, A. Klimas, and M. Kuznetsova, Phys. Rev. Lett. **106**, 195003 (2011).
[47]M. Hesse and D. Winske, J. Geophys. Res. **99**, 11177, https://doi.org/10.1029/94JA00676 (1994).
[48]P. L. Pritchett, J. Geophys. Res. **106**, 3783, https://doi.org/10.1029/1999JA001006 (2001).
[49]K. Fujimoto, Phys. Plasmas **13**, 072904 (2006).
[50]A. Klimas, M. Hesse, S. Zenitani, and M. Kuznetsova, Phys. Plasmas **17**, 112904 (2010).
[51]N. Bessho, L.-J. Chen, J. Shuster, and S. Wang, Geophys. Res. Lett. **41**, 8688, https://doi.org/10.1002/2014GL062034 (2014).
[52]A. Klimas, Phys. Plasmas **22**, 042901 (2015).
[53]A. Klimas, M. Hesse, and S. Zenitani, Phys. Plasmas **19**, 042901 (2012).
[54]S. Zenitani, H. Hasegawa, and T. Nagai, J. Geophys. Res. (Space Phys.) **122**, 7396, https://doi.org/10.1002/2017JA023969 (2017); e-print arXiv:1702.07244 [physics.plasm-ph].
[55]J. Egedal, B. Wetherton, W. Daughton, and A. Le, Phys. Plasmas **23**, 122904 (2016).
[56]M. Hesse, S. Zenitani, and A. Klimas, Phys. Plasmas **15**, 112102 (2008).
[57]S. Zenitani, I. Shinohara, T. Nagai, and T. Wada, Phys. Plasmas **20**, 092120 (2013).
[58]S. Markidis, G. Lapenta, G. Delzanno, P. Henri, M. Goldman, D. Newman, T. Intrator, and E. Laure, Plasma Phys. Controlled Fusion **56**, 064010 (2014).
[59]T. Nakamura, R. Nakamura, and H. Hasegawa, Ann. Geophys. **34**, 357 (2016).
[60]N. Aunai, M. Hesse, and M. Kuznetsova, Phys. Plasmas **20**, 092903 (2013).

[61]A. Zeiler, D. Biskamp, J. F. Drake, B. N. Rogers, M. A. Shay, and M. Scholer, J. Geophys. Res. (Space Phys.) **107**, 1230, https://doi.org/10.1029/2001JA000287 (2002).
[62]M. Hesse, N. Aunai, J. Birn, P. Cassak, R. Denton, J. Drake, T. Gombosi, M. Hoshino, W. Matthaeus, D. Sibeck *et al.*, Space Sci. Rev. **199**, 577 (2016).
[63]O. Chapurin and A. Smolyakov, J. Appl. Phys. **119**, 243306 (2016).
[64]M. Shay and M. Swisdak, Phys. Rev. Lett. **93**, 175001 (2004).
[65]D. B. Korovinskiy, V. S. Semenov, N. V. Erkaev, A. V. Divin, and H. K. Biernat, J. Geophys. Res. (Space Phys.) **113**, A04205, https://doi.org/10.1029/2007JA012852 (2008).
[66]J. Egedal, A. Le, and W. Daughton, Phys. Plasmas **20**, 061201 (2013).
[67]A. Le, J. Egedal, W. Daughton, W. Fox, and N. Katz, Phys. Rev. Lett. **102**, 085001 (2009).